## 8

#### Review article

Ingo Gregor\*, Alexey Chizhik, Narain Karedla and Jörg Enderlein

# Metal-induced energy transfer

https://doi.org/10.1515/nanoph-2019-0201 Received June 27, 2019; revised July 29, 2019; accepted August 2,

Abstract: Since about a decade, metal-induced energy transfer (MIET) has become a tool to measure the distance of fluorophores to a metal-coated surface with nanometer accuracy. The energy transfer from a fluorescent molecule to surface plasmons within a metal film results in the acceleration of its radiative decay rate. This can be observed as a reduction of the molecule's fluorescence lifetime which can be easily measured with standard microscopy equipment. The achievable distance resolution is in the nanometer range, over a total range of about 200 nm. The method is perfectly compatible with biological and even live cell samples. In this review, we will summarize the theoretical and technical details of the method and present the most important results that have been obtained using MIET. We will also show how the latest technical developments can contribute to improving MIET, and we sketch some interesting directions for its future applications in the life sciences.

Keywords: energy transfer; fluorescence lifetime; fluorescence lifetime imaging microscopy; super-resolution microscopy; surface plasmons; time-correlated singlephoton counting.

**PACS:** 78.20.-e; 78.66.-w; 78.47.jb; 78.67.Wj; 78.67.+m; 87.64.M-; 87.80.Nj.

\*Corresponding author: Ingo Gregor, Third Institute of Physics-Biophysics, Georg August University, Friedrich-Hund-Platz 1, 37077 Göttingen, Germany, e-mail: ingo.gregor@phys.uni-goettingen.de. https://orcid.org/0000-0002-1775-2159

Alexey Chizhik: Third Institute of Physics-Biophysics, Georg

August University, Göttingen, Germany

Narain Karedla: Physical and Theoretical Chemistry, University of Oxford, Oxford OX1 3TA, UK

Jörg Enderlein: Third Institute of Physics-Biophysics, Georg August University, Göttingen, Germany; and Cluster of Excellence "Multiscale Bioimaging: From Molecular Machines to Networks of Excitable Cells" (MBExC), Georg August University, Göttingen, Germany

### 1 Introduction

Surprisingly, the emission process of almost all fluorescent molecules can be excellently described by the classical theory of an electric dipole emitter. One can thus use Maxwell's classical theory of electromagnetism to describe the electrodynamic interaction of fluorescent molecules with complex dielectric and/or metallic environments. One of the most striking predictions of this theoretical description is that the radiative rate of a fluorophore depends on the geometry and dielectric properties of its surrounding [1]. In other words, the dielectric properties of the environment have a direct impact on the emission properties of a fluorescing molecule. The situation becomes even more complex for structured environments, such as interfaces [2, 3], cylindrical nanocavities (zero mode waveguides) [4, 5], or spherical nanocavities [6, 7]. Another well-known example is Förster resonance energy transfer (FRET) [8, 9], where the electromagnetic near-field coupling between a donor and an acceptor molecule leads to a dramatic change of the radiative decay rate of the donor.

In the 1960s and 1970s, a series of remarkable and elegant experiments by Kuhn and Drexhage demonstrated the striking effect of a reflecting mirror on the fluorescence of molecules in close proximity [10-17]. They observed changes in the angular distribution of emission as well as in the spontaneous decay rate of the fluorescent molecules. At that time, they could qualitatively explain the effects using a classical interference model. Quite soon after, Silbey and co-workers developed a complete semi-classical theory which described these experiments quantitatively and with high accuracy [18]. Although this exquisite agreement between a semi-classical model based on Maxwell's equations and the experiments by Kuhn and Drexhage was (and is) considered to be a superb example of fundamental science, not much practical applications of these phenomena were seen then. However, when considering that Drexhage used the stacks of lipid mono-layers (~3 nm) as spacers of well-defined thickness between the molecules and the mirror, the potential of the effect for modern microscopy becomes immediately apparent.

Fluorescence microscopy combines highest sensitivity with molecular specificity and exceptional image contrast. Therefore, it has become an extremely versatile and powerful research tool for numerous studies in the life and material sciences. However, the spatial resolution of classical fluorescence microscopy is limited by the diffractive nature of light to about 200 nm laterally and 500 nm axially. Nowadays, super-resolution fluorescence microscopy routinely overcomes this limit. However, for almost all super-resolution techniques, the difference of three- to five-fold between lateral and axial resolution remains. To achieve a similar axial as lateral resolution remains challenging. Reflection interference contrast microscopy [19] or interferometric scattering microscopy [20] can achieve nanometer localization accuracy along the optical axis, but these methods lack the specificity and, to some extent, the sensitivity of fluorescence microscopy methods. Various fluorescence-based techniques have been proposed to gain super-resolution along the optical axis. Single-molecule localization methods such as stochastic optical reconstruction microscopy (STORM) and photoactivated localization microscopy (PALM) achieve an accuracy in the order of ~50 nm along the optical axis using astigmatic imaging [21] or biplane imaging [22]. Using point-spread function shaping [23] one can accomplish an accuracy in the range of 10–20 nm. Two other techniques are variable-angle total internal reflection fluorescence microscopy [24, 25] and super-critical angle fluorescence imaging [26, 27]. Not based on single-molecule localization, these methods do achieve an axial resolution of approximately 10 nm. Two techniques that perform even better are interferometric PALM [28] and 4pi-STORM [29]. They reach nanometer axial single-molecule localization accuracy, but for the prize of extreme technical complexity and difficult applicability for routine biological research. Moreover, they require special photo-switchable dyes or proteins (photo-activatable fluorescent proteins) when applied to imaging. In a recent preprint, the group of Stefani carefully analyzed the brightness of single emitters under STORM conditions excited using an evanescent field [30]. The strong dependence of the brightness allowed the localization of the 3D positions with an accuracy of 10 nm in 3D.

Here, we present a simple and reliable method, metalinduced energy transfer (MIET) imaging, for axial localization of fluorescence molecules with nanometer accuracy. The principle of MIET imaging is based on the energy transfer from a fluorescent molecule to surface plasmons within a thin metal film on a glass surface, which results in the acceleration of its spontaneous decay rate. This can be observed as a reduction of the molecule's fluorescence lifetime. Within the first 200 nm above the metal film, the energy transfer rate is monotonically dependent on the distance of a molecule from the metal layer. Thus, within this distance range, a measured fluorescence lifetime can be uniquely converted into a distance between the emitter and the surface.

## 2 Theoretical background

As already mentioned, the emission process of most fluorescent molecules is excellently described by the model of an ideal electric dipole emitter. Following Chance et al. [31], a semi-classical modeling of the electromagnetic interaction of an emitting molecule with its environment is based on solving Maxwell's equations for the electromagnetic field in the given environment with the dipole emitter as the field's source.

For a planar stratified environment, the geometry of the considered situation is shown in Figure 1. The emitting

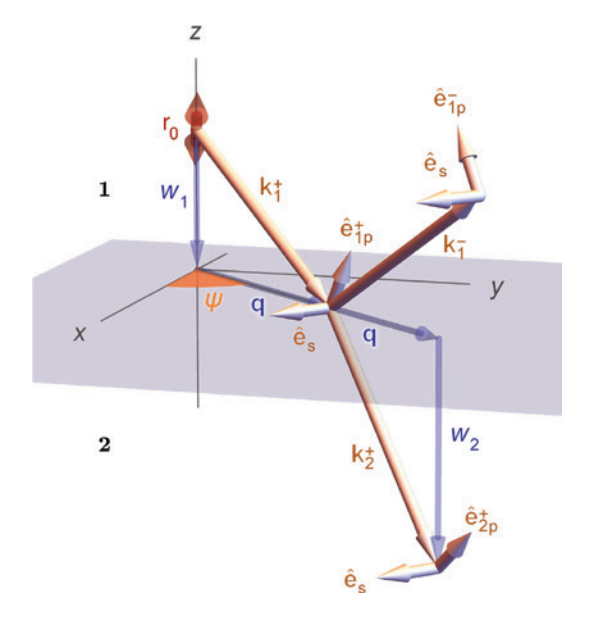


Figure 1: General geometry of dipole emission above an interface. An oscillating electric dipole (red double arrow) is located at position  $\mathbf{r}_0 = (\boldsymbol{\rho}_0, \boldsymbol{z}_0)$  within medium "1" above an interface dividing it from a medium "2" below the interface. The figure shows the vectors that define one of the plane waves that contribute to the dipole's electromagnetic emission. The wave vector of a directly emitted wave is  $\mathbf{k}_{1}^{+}$ , and the wave vector of its reflection from the interface is  $\mathbf{k}_1^-$ . The unit vectors  $\hat{\mathbf{e}}_{1n}^\pm$  represent the directions of the electric field vector in the plane of incidence (p-polarization), whereas the unit vector ê, points in the direction perpendicular to the plane of incidence (s-polarization). Shown are also the wave vector and the p- and s-polarization vectors of the plane wave transmitted into medium "2". The projections of all wave vectors into the interface are all equal and denoted by q. The projections along the vertical zaxis are  $\pm w_1$  and  $w_2$ . The angle  $\psi$  is the angle between the horizontal projections **q** of all wave vectors and the x-axis. The "interface" itself can be any stack of planar layers of different materials.

molecule (electric dipole emitter) is located at position  $\mathbf{r}_0 = (x_0, y_0, z_0) = (\boldsymbol{\rho}_0, z_0)$  in a medium with refractive index  $n_1$ . In this medium, Maxwell's equations lead to the following determining equation for the electric field **E** at position **r**:

rot rot 
$$\mathbf{E}(\mathbf{r}) - k_1^2 \mathbf{E}(\mathbf{r}) = 4\pi k_0^2 \mathbf{p} \,\delta \,(\mathbf{r} - \mathbf{r}_0).$$
 (1)

On the right-hand side, the dipole emitter source is represented as the Dirac delta function. The wave vector amplitudes  $k_1 = n_1 k_0$  refer to medium 1 and the vacuum, respectively. Let us first consider only an infinitely extended homogeneous medium 1. Then, in Fourier space, the solution  $\tilde{\mathbf{E}}$  of the last equation is found as follows:

$$\tilde{\mathbf{E}}(\mathbf{k}) = \frac{4\pi}{n_1^2} \frac{k_1^2 \mathbf{p} - \mathbf{k}(\mathbf{k} \cdot \mathbf{p})}{k^2 - k_1^2} \exp(-i\mathbf{k} \cdot \mathbf{r}_0), \qquad (2)$$

where a tilde denotes the Fourier transform. The field in real space is then found by an inverse Fourier transform. Using Cartesian coordinates,  $\mathbf{k} = (q_v, q_v, w) = (\mathbf{q}, w)$ , we can integrate over w applying Cauchy's residue theorem. Here, only the poles  $W_1 = +(k_1^2 - q^2)^{1/2}$  will be taken into account so that the solution automatically consists of only outgoing plane waves. This integration results in the so-called Weyl representation of the electric field of an oscillating electric dipole:

$$\mathbf{E}(\mathbf{r}) = \frac{i}{2\pi n_1^2} \int \frac{\mathrm{d}^2 \mathbf{q}}{w_1} [k_1^2 \mathbf{p} - \mathbf{k}_1^{\pm} (\mathbf{k}_1^{\pm} \cdot \mathbf{p})] \cdot \exp\{i[\mathbf{q} \cdot (\boldsymbol{\rho} - \boldsymbol{\rho_0}) + w_1 | z - z_0 |]\},$$
(3)

where  $\mathbf{k}_{1}^{\pm} = (\mathbf{q}, \mp w_{1})$  refers to the wave vectors above  $(z>z_0)$  and below  $(z<z_0)$  the emitter's position, respectively. The two-dimensional integration  $d^2\mathbf{q}$  extends over the whole **q**-plane; see Figure 1. This Weyl representation of the electric field is a superposition of plane waves and is thus ideally suited to study next the interaction of the dipole field with a planar horizontal interface (z=0).

To model such an interaction, we will use Fresnel's formulas for the reflection and transmission coefficients of a plane electromagnetic wave interacting with an interface [32]. These coefficients are polarization dependent, and we thus separate the plane waves in Eq. (3) into their s- and p-polarization components (electric field vector either perpendicular or within the plane of incidence formed by the wave vector and the normal to the interface, respectively). The corresponding unit vectors of the electric field polarization are given by (see also Figure 1)

$$\hat{\mathbf{e}}_{s} = \left(\frac{-q_{y}}{q}, \frac{q_{x}}{q}, 0\right) \text{ and } \hat{\mathbf{e}}_{lp}^{\pm} = \frac{\pm w_{l}}{k_{l}q} \left(q_{x}, q_{y}, \frac{q^{2}}{\pm w_{l}}\right).$$

They are both perpendicular to the wave vector  $\mathbf{k}$ , while  $\hat{\mathbf{e}}_{s}$  is parallel to the interface (s-wave);  $\hat{\mathbf{e}}_{1n}^{\pm}$  lies within the plane of incidence (p-wave). Thus, we can re-write Eq. (3) as follows:

$$\mathbf{E}(\mathbf{r}) = \frac{ik_0^2}{2\pi} \iint \frac{\mathrm{d}^2 \mathbf{q}}{w_1} [\hat{\mathbf{e}}_{1p}^{\pm} (\hat{\mathbf{e}}_{1p}^{\pm} \cdot \mathbf{p}) + \hat{\mathbf{e}}_{s} (\hat{\mathbf{e}}_{s} \cdot \mathbf{p})] \cdot \exp\{i[\mathbf{q} \cdot (\boldsymbol{\rho} - \boldsymbol{\rho_0}) + w_1 | z - z_0 |]\}.$$
(4)

In this way, we have obtained, with (4), an expansion of the dipole's electric field into plane p- and s-waves. Note that for  $\mathbf{q}$ -vectors where  $w_1$  becomes purely imaginary  $(q>k_1)$ , the plane wave amplitude decays exponentially with increasing distance from the dipole. Using Fresnel's well-known relations, Eq. (4) now allows us to directly write down an expression for the reflected field (z>0):

$$\mathbf{E}_{R}(\mathbf{r}) = \frac{ik_{0}^{2}}{2\pi} \iint \frac{\mathrm{d}^{2}\mathbf{q}}{w_{1}} [\hat{\mathbf{e}}_{1p}^{-}R_{p}(\hat{\mathbf{e}}_{1p}^{+} \cdot \mathbf{p}) + \hat{\mathbf{e}}_{s}R_{s}(\hat{\mathbf{e}}_{s} \cdot \mathbf{p})] \cdot \exp \left\{ i[\mathbf{q} \cdot (\boldsymbol{\rho} - \boldsymbol{\rho}_{0}) + w_{1}z_{0} + w_{1}z] \right\},$$
(5)

with  $R_{\rm n,s}$  denoting Fresnel's reflection coefficients for p- and s-waves, respectively. Similarly, the electric field transmitted through the interface at z<0 into medium  $n_z$ is given by

$$\mathbf{E}_{\mathrm{T}}(\mathbf{r}) = \frac{ik_{0}^{2}}{2\pi} \iint \frac{\mathrm{d}^{2}\mathbf{q}}{w_{1}} [\hat{\mathbf{e}}_{2p}^{+} T_{p} (\hat{\mathbf{e}}_{1p}^{+} \cdot \mathbf{p}) + \hat{\mathbf{e}}_{s} T_{s} (\hat{\mathbf{e}}_{s} \cdot \mathbf{p})] \cdot \exp \left\{ i[\mathbf{q} \cdot (\boldsymbol{\rho} - \boldsymbol{\rho}_{0}) + w_{1} z_{0} - w_{2} z] \right\}.$$
(6)

Here, the unit vector

$$\hat{\mathbf{e}}_{2p}^{+} = \frac{w_2}{k_2 q} \left( q_x, q_y, \frac{q^2}{w_2} \right)$$

is perpendicular to the wave vector in medium 2 where the wave vector is given by  $\mathbf{k}_{2}^{+} = \{q_{x}, q_{y}, -w_{2}\}$  (Snell's law), with  $W_2 = (k_2^2 - q^2)^{1/2}$  and  $T_{p,s}$  being Fresnel's transmission coefficients. The phase  $\exp(iw_1z_0)$  in  $\mathbf{E}_{\mathrm{R}}$  and  $\mathbf{E}_{\mathrm{T}}$  accounts for the wave propagation from the dipole's position to the interface.

The magnitude of both fields depends on the orientation of the dipole vector **p** with respect to the interface, as is captured by the scalar products  $\hat{\mathbf{e}}_{1n}^{\pm} \cdot \mathbf{p}$  and  $\hat{\mathbf{e}}_{s} \cdot \mathbf{p}$  in the above equations. The reflection and transmission coefficients  $T_{p,s}$  and  $R_{p,s}$  are functions of the refractive indices  $n_1$  and  $n_2$  and the angle of incidence (and thus q) of the plane waves to the interface. It should be emphasized that expressions (5) and (6) are applicable to a general stratified stack of planar layers between the emitter and a homogeneous medium below - in that case, one has to only replace the Fresnel coefficients for a single interface by those for the stratified stack.

Now, using (6), it is easy to determine the total energy emission of the emitter into the bottom half space. Note that the electric field vector of each plane-wave component traveling along the wave vector  $\mathbf{k}_1 = \{\mathbf{q}, -w_1\}$  is indeed perpendicular to  $\mathbf{k}_2$ , since  $\mathbf{k}_2 \perp \hat{\mathbf{e}}_{2p}^+$  and  $\mathbf{k}_2 \perp \hat{\mathbf{e}}_s$ . Furthermore, all plane-wave components with  $Im(w_2) > 0$ decay exponentially and do not contribute to the far-field radiation. For wave components where  $w_2$  is real, that is,  $q \le k_1$ , we can rewrite **q** and  $w_2$  in terms of the emission angles  $\psi$  and  $\theta$  and find  $\mathbf{q} = k_2 \{ \sin \theta \cos \psi, \sin \theta \sin \psi, 0 \}$ and  $w_2 = k_2 \cos \theta$ . Here,  $\theta$  is the angle between the downward vertical axis and  $\mathbf{k}$ , and  $\psi$  is the angle between the *x*-axis and the projection of  $\mathbf{k}$ , into the (x, y)-plane. We also find  $\hat{\mathbf{e}}_{2p}^{+} = \left\{\cos\theta \cos\psi, \cos\theta \sin\psi, \sin\theta\right\}$  and  $\hat{\mathbf{e}}_{s} = \left\{\sin\psi, -\cos\psi, 0\right\}$ . For an emitter on the optical axis  $(\boldsymbol{\rho}_{0} = 0)$ , (6) shows that the electric field amplitude vector connected with emission into the solid angle  $\sin \theta d\theta d\psi$  is proportional to

$$\frac{ik_0^3}{2\pi}\frac{w_2}{w_1}[\hat{\mathbf{e}}_{2p}^+T_p(\hat{\mathbf{e}}_{1p}^+\cdot\mathbf{p})+\hat{\mathbf{e}}_sT_s(\hat{\mathbf{e}}_s\cdot\mathbf{p})]\exp(iw_1z_0).$$

Knowing this electric field amplitude, we can find the time-averaged energy flux density (Poynting vector) as follows:

$$P_{-}(\theta, \psi) = \frac{cn_{2}}{8\pi} |E|^{2}$$

$$\propto \frac{ck_{0}^{6}n_{2}}{32\pi^{3}} [|T_{p}|^{2} (\hat{\mathbf{e}}_{1p}^{+} \cdot \mathbf{p})^{2} + |T_{s}|^{2} (\hat{\mathbf{e}}_{s}^{+} \cdot \mathbf{p})^{2}] \cdot \left| \frac{w_{2}}{w_{1}} \right|^{2}$$

$$= \exp(-2\text{Im}(w_{1})z_{0}),$$

where the proportionality factor is found by comparing this result with the emission of a free dipole  $S_0 = ck_0^4 n_1 p^2 / 3$ , which then yields

$$P_{-}(\theta, \psi) = \frac{ck_0^4 n_2}{8\pi} [|T_{\rm p}|^2 (\hat{\mathbf{e}}_{1\rm p}^+ \cdot \mathbf{p})^2 + |T_{\rm s}|^2 (\hat{\mathbf{e}}_{\rm s} \cdot \mathbf{p})^2] \cdot \left| \frac{w_2}{w_1} \right|^2 \\ \exp(-2\text{Im}(w_1)z_0).$$

A similar equation can be derived, starting from (4) to (5), for the emission into the upper half-space:

$$P_{+}(\theta, \psi) = \frac{ck_{0}^{4}n_{1}}{8\pi} [|(\hat{\mathbf{e}}_{1p}^{-} + R_{p}\hat{\mathbf{e}}_{1p}^{+} e^{2iw_{1}z_{0}}) \cdot \mathbf{p}|^{2} + |(1 + R_{s}e^{2iw_{1}z_{0}}) \cdot \hat{\mathbf{p}}|^{2}],$$

where  $\theta$  is now the angle between the propagation direction and the vertical +z-axis.

The total emission per unit time from the dipole is obtained by integrating over the respective half spheres.

$$S(\alpha, z_0) = \int_{0}^{\pi/2} d\theta \sin \theta \int_{0}^{2\pi} d\psi (P_{-}(\theta, \psi) + P_{+}(\theta, \psi)).$$

To clarify the dependence on the elevation angle  $\alpha$  we first consider the special case of a vertical dipole,  $\alpha = 0$ , or  $\mathbf{p} = p\hat{\mathbf{e}}_z$ . Using  $(\hat{\mathbf{e}}_{1p}^+ \cdot \hat{\mathbf{e}}_z) = (\hat{\mathbf{e}}_{1p}^- \cdot \hat{\mathbf{e}}_z) = q/k_1$  we find

$$S_{\perp} = \frac{ck_0p^2}{2n_1^2} \operatorname{Re} \left\{ \int_0^{\infty} \frac{\mathrm{d}qq^3}{w_1} (1 + R_p e^{2iw_1z_0}) \right\}.$$

Similarly, for a parallel dipole  $\alpha = \pi/2$ , or  $\mathbf{p} = p\hat{\mathbf{e}}_{\cdot}$ , we

$$S_{\parallel} = \frac{ck_0^3 p^2}{4} \operatorname{Re} \left\{ \int_0^{\infty} \frac{\mathrm{d}q \, q}{w_1} \left[ \frac{w_1^2}{k_1^2} (1 - R_{\mathrm{p}} e^{2iw_1 z_0}) + (1 + R_{\mathrm{s}} e^{2iw_1 z_0}) \right] \right\},$$

taken  $(\hat{\mathbf{e}}_{1n}^+ \cdot \hat{\mathbf{e}}_x) = -(\hat{\mathbf{e}}_{1n}^- \cdot \hat{\mathbf{e}}_x) = w_1 / k_1 \cos \psi$  and  $(\hat{\mathbf{e}}_s \cdot \hat{\mathbf{e}}_x) = \sin \psi$ , with  $\psi$  being the angle between the x-axis and the vector **q**, and furthermore, that the average of  $\cos^2 \psi$  and  $\sin^2 \psi$  over the full circle is both 1/2. Finally, the emission rate of a dipole oriented at an arbitrary angle  $\alpha$  with respect to the normal of the surface and at height  $z_0$  can be written as follows:

$$S(\alpha, z_0) = S_{\perp}(z_0)\cos^2\alpha + S_{\parallel}(z_0)\sin^2\alpha.$$
 (7)

The average lifetime  $\tau_{_{\mathrm{fl}}}$  of an ideal dipole will be inversely proportional to the just calculated emission rate. However, the fluorescence quantum yield  $\eta$  of real dyes is lower than 1, and the ratio of the lifetime  $\tau_{_{\mathrm{fl}}}$  in the presence of an interface to the lifetime  $\tau_0$  within a homogeneous medium is given by

$$\frac{\tau_{\rm fl}(\alpha, z)}{\tau_{\rm o}} = \frac{S_{\rm o}}{\eta S(\alpha, z) + (1 - \eta)S_{\rm o}},\tag{8}$$

where  $S_0$  is the radiative emission rate in free space with the refractive index  $n_1$  and far away from any dielectric or metal interfaces. Since a fluorescent molecule emits a spectrum of frequencies, one has to calculate the values of *S* over the full spectral range of the dye and average the result with the normalized emission spectrum as weight function. Often, we are interested in the lifetime of a dye which can freely rotate, with a rotational diffusion time much faster than the typical fluorescence decay time. In that case, one can average the decay rate, Eq. (7), over all orientations:

$$\overline{S(z_0)} = \langle S(\alpha, z_0) \rangle_{\alpha} = \frac{1}{3} [S_{\perp}(z_0) + 2S_{\parallel}(z_0)]. \tag{9}$$

Eq. (8) is the theoretical basis of MIET; it establishes a direct relationship between the measurable fluorescence lifetime and the vertical position of a fluorescing molecule above a surface. Note that there is no free fitting parameter entering this relationship. All involved quantities are welldefined absolute physical or geometric properties.

Nonetheless, the calculations of the Fresnel coefficients for arbitrary multi-layered structures and the integration over the electric field amplitude vectors require some numerical effort. We have developed a freely available software tool that allows anyone to calculate the distance dependence of the fluorescence lifetime for arbitrary planar sample structures; see [33].

## 3 Instrumentation and applications

The measurement of the distance of a fluorophore from a metal surface is fairly simple. However, there are some prerequisites that have to be met beforehand. First of all, one needs a suitable sample substrate. Second, for the selected fluorophore, one needs to know the fluorescence quantum yield in a homogeneous medium, having comparable properties as the sample of interest, typically aqueous buffer. Preferentially, the fluorophore has a mono-exponential lifetime in this medium. Finally, one needs an instrument to record a fluorescence lifetime image of the labeled sample on the MIET substrate. In the following, we discuss the details of these various issues.

#### 3.1 MIET substrate

In principle, the substrate consists of a microscopic glass coverslip (thickness = 170  $\mu$ m, refractive index n = 1.52). For most dyes, gold is a very well-suited metal for doing MIET. Typically, we evaporate a 2-nm titanium layer on the glass to bond a film of 10- to 15-nm gold firmly to the surface. If an additional SiO<sub>2</sub> coating is needed, we additionally evaporate another 1-nm of titanium, before we deposit a 10-nm layer of silica on top. This silica spacer on top is sometimes needed to avoid direct contact of a fluorophore or biological sample with the metal. The complex-valued refractive indices of the metal layer as a function of wavelength are either taken from publications or have to be measured with ellipsometry. In principle, one can use any metal or alloy that has a suitable (imaginary) refractive index in the spectral range of the emission of the fluorophore and is sufficiently transparent in the spectral range used. However, one has to ensure that the film is homogeneous in thickness and composition over a large area. For biological samples, gold is preferable because of its chemical inertness.

As an example, we calculated the fluorescence lifetime of an emitter at  $\lambda_{em}$  = 690 nm emission wavelength as a function of the distance and its quantum yield. The emitter is placed in water (refractive index  $n_1 = 1.33$ ). The result is shown in Figure 2 for 10 different values of quantum vield  $\eta$ .

The sample preparation on such a MIET substrate is exactly the same as for normal glass coverslips. In order to measure the lifetime of the fluorescent label without the MIET effect (the so-called free-space lifetime), we recommend to have a parallel sample preparation on normal glass substrates. Alternatively, one can measure the free-space lifetime by focusing the objective lens several micrometers above the gold layer, where the effect of MIET becomes negligible.

#### 3.2 Quantum yield and free-space lifetime

As mentioned, it is necessary to know the fluorescence lifetime of the fluorescent probe as reference. Ideally, this reference is obtained under the same conditions, as are present in the MIET measurements. This means that it

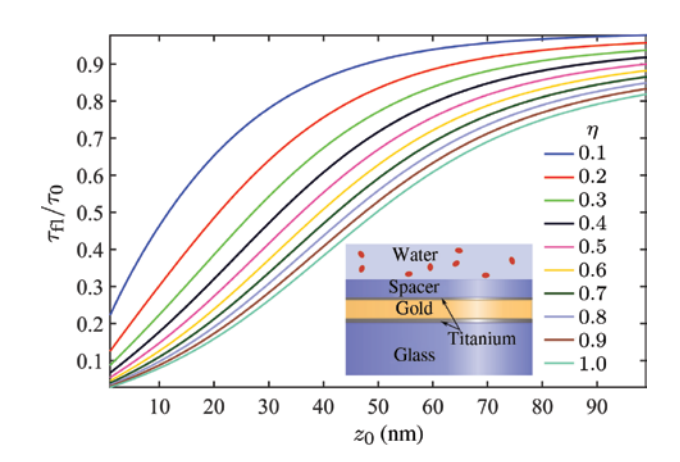


Figure 2: Exemplary MIET curves.

A fluorescent emitter is placed in water (refractive index  $n_1 = 1.33$ ) on top of an MIET substrate. The MIET substrate consists of glass  $(n_2 = 1.52)$  which is covered by 2-nm titanium  $(n_{T_1} = 2.18 + 3.27i)$ , 10-nm gold ( $n_{AII} = 0.17 + 3.79i$ ), and 1-nm titanium that is topped with a layer of 10-nm  $SiO_2(n_{SiO_2} = 1.46)$ . All refractive indices are given for the emission wavelength  $\mathring{\lambda}_{\rm em} = 690$  nm. Shown is the fluorescence lifetime  $\tau_{\rm q}$  relative to the lifetime in pure water  $\tau_{\rm o}$  of the emitter as a function of the distance from the surface  $(z_0)$  and its quantum yield  $(\eta = 0.1-1.0)$ . Data taken from [34].

should be labeled to the same structure of interest, at the same concentration, and in the same medium, etc. Unspecific labeling and excess of free dye should be avoided. Under optimal conditions, one obtains a uniform monoexponential fluorescence decay for the reference sample. There should be no detectable variation of the lifetime within the field of view.

A second requirement is to know the quantum yield of fluorescence  $\eta$  associated with the determined lifetime  $\tau_{\rm fl}$ . There is an accurate method to determine this quantum vield that requires only minimal amounts of sample [35]. Of course, one can also use the more classic method of comparing the emission strength relative to a known standard. If the quantum yield of the label is known in some specific medium, one can infer it by the ratio of the fluorescence lifetimes the quantum yield of the probe as  $\eta = \eta_{\text{ref}} n^2 \tau_{\text{fl}} / (n_{\text{ref}}^2 \tau_{\text{ref}})$ . Here,  $\eta_{\text{ref}}$ ,  $\tau_{\text{ref}}$ , and  $n_{\text{ref}}$  are the fluorescence quantum yield, lifetime, and the refractive index of the reference solution, respectively. This method relies on the assumption that the non-radiative rate of the dye changes only upon modification of its local chemical environment, while the change in the refractive index of the medium modifies the radiative rate. Although this equation may not hold in rare specific complex cases, it allows one to reliably estimate the quantum yield for most of the samples.

#### 3.3 FLIM measurements

The measurement of the fluorescent lifetime images can be done using basically any fluorescence lifetime imaging microscopy (FLIM) technique. Most favorably, one uses a scanning confocal microscope with pulsed laser excitation and time-correlated single-photon counting. However, time-gated cameras or frequency domain-based modulated cameras work as well. Two-photon excited fluorescence is a popular technique used for FLIM. In combination with gold-coated MIET substrates, one has to take care that the intrinsic absorption in the NIR range does not lead to thermal damage in the film.

From frequency-based measurements, one obtains an average fluorescence lifetime  $\tau_{av}$ . If the fluorophores in the pixel have the same height z, one can correctly convert  $\tau_{aa}$ into z based on the MIET curve.

From the time-domain measurements, one obtains the fluorescence lifetime values usually by pixel-wise fitting of the decays. For a simple analysis, one can also use the average fluorescence decay time. However, especially in the case of single-molecule experiments, a proper fitting of the decay histogram can discern lifetimes of at least two emitters in the same focal spot. In principle, the MIET curve not only determines the lifetime as a function of height, but also the brightness of the emitter. This fixes the ratio of the amplitudes in a multi-exponential fit, which clearly improves the accuracy of such analysis.

#### 3.3.1 Super-resolution methods and MIET

The first proof-of-principle study of MIET was carried out by Diez et al. in 2010 [36]. Using a wide-field two-photon excitation and a time-gated camera, they determined the height of microtubules that were formed by AlexaFluor 488 labeled  $\alpha$ -tubulin. The microtubules have a peculiar geometry that resemble long cylinders with diameter 25 nm lying flat on the surface. Accounting for an even fluorophore distribution around the perimeter of the microtubules, the distance of the fluorescent microtubules from the gold surface (measured from the top of the surface to the bottom of the microtubules) was determined. Different modifications were tested to ensure that the microtubules had different heights. At first, labeled microtubules were fixed by electrostatic interaction with avidin to the surface, which resulted in a height of 7.5(10) nm (standard error of the mean). Next, microtubules were biotinylated and bound to neutravidin before they were fixed to the surface using avidin, which resulted in a height of 13.3(15) nm. Finally, microtubules were linked to kinesin-1 motor proteins that were immobilized on the surface. For this, a height of 26.4(9) nm was found. The obtained resolution of the height was clearly better than the size of the involved proteins.

Chizhik et al. used MIET to measure the profile of the basal cell membrane of live cells [37], see Figure 3. Using a specific membrane dye ensured that the fluorescence originated exclusively from the membrane of the cells. Distinct differences between different cell lines were observed. Also, it was possible to follow the cells over time and observe how the cells attach and spread on the surface of the slide. Later, this technique was used to follow the induced transition of epithelial cells into a mesenchymal state over a time course of up to 40 h [38]. The transition involves a noticeable rise of the cells by about 20-30 nm within less than 6 h followed by a relatively slow relaxation to the original height over about 20 h.

By immuno-staining Lap2 and Nup358, specific proteins at the inner and outer nuclear membrane were labelled with AlexaFluor 488 and AlexaFluor 633, respectively, Chizhik et al. were able to determine the 3D profile of the two membranes over the whole basal area [39]. They measured a relatively constant distance of about 30 nm, where the roughness of the inner nuclear membrane was more pronounced than that of the outer membrane. The

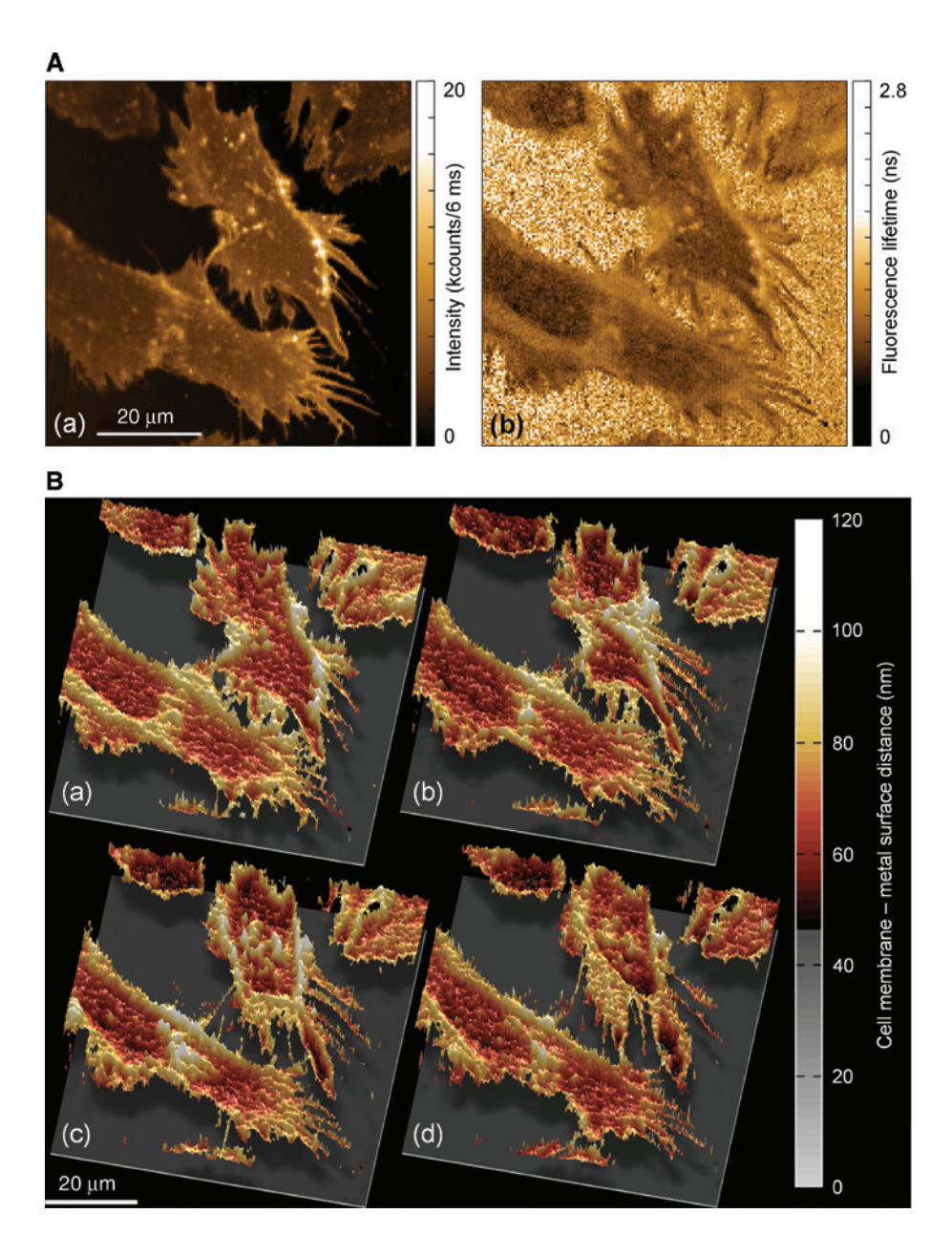


Figure 3: Height profiling of the basal membrane of adherent cells. (A) Simultaneously acquired fluorescence intensity (a) and lifetime (b) images of the basal membrane of living MDA-MB-231 cells grown on a gold-covered glass substrate and stained with CellMask Deep Red plasma membrane stain (Invitrogen). (B) Three-dimensional profiles computed from fluorescence lifetime images sequentially recorded with 10-min delays. Data taken from [37].

obtained thickness of the nuclear envelope is in very good agreement with the values obtained using electron microscopy.

The group of Rehfeldt used two-color MIET to determine the 3D architecture of focal adhesions [40]. Specifically, they looked at actin and vinculin in the first 24 h after seeding human mesenchymal stem cells. The twocolor staining allowed measuring the heights of the proteins using MIET, as well as their distance via FRET.

Using graphene as a metal-like substrate, Ghosh et al. determined the thickness of lipid bilayers by localizing the fluorescently labeled lipids above the substrate with a precision of less than a nanometer [41]. The difference of the positions for the upper and lower leaflet reveals the height of the bilayer. Graphene is a very well working MIET substrate in the range of up to 25 nm. In this range it can provide a better resolution than gold.

These examples show that MIET can be used as a nanometer-precise super-resolution technique in fluorescence imaging. Using relatively simple means, one can obtain valuable additional information with very high precision.

#### 3.3.2 Single-molecule MIET

In 2014, Karedla et al. presented smMIET, which uses fluorescence lifetime information to determine the distance

between a single molecule and a metallized surface [42], see Figure 4. In combination with orientation measurements, smMIET can determine distance values with accuracy better than 2.5 nm. As in the case of FRET, it also needs

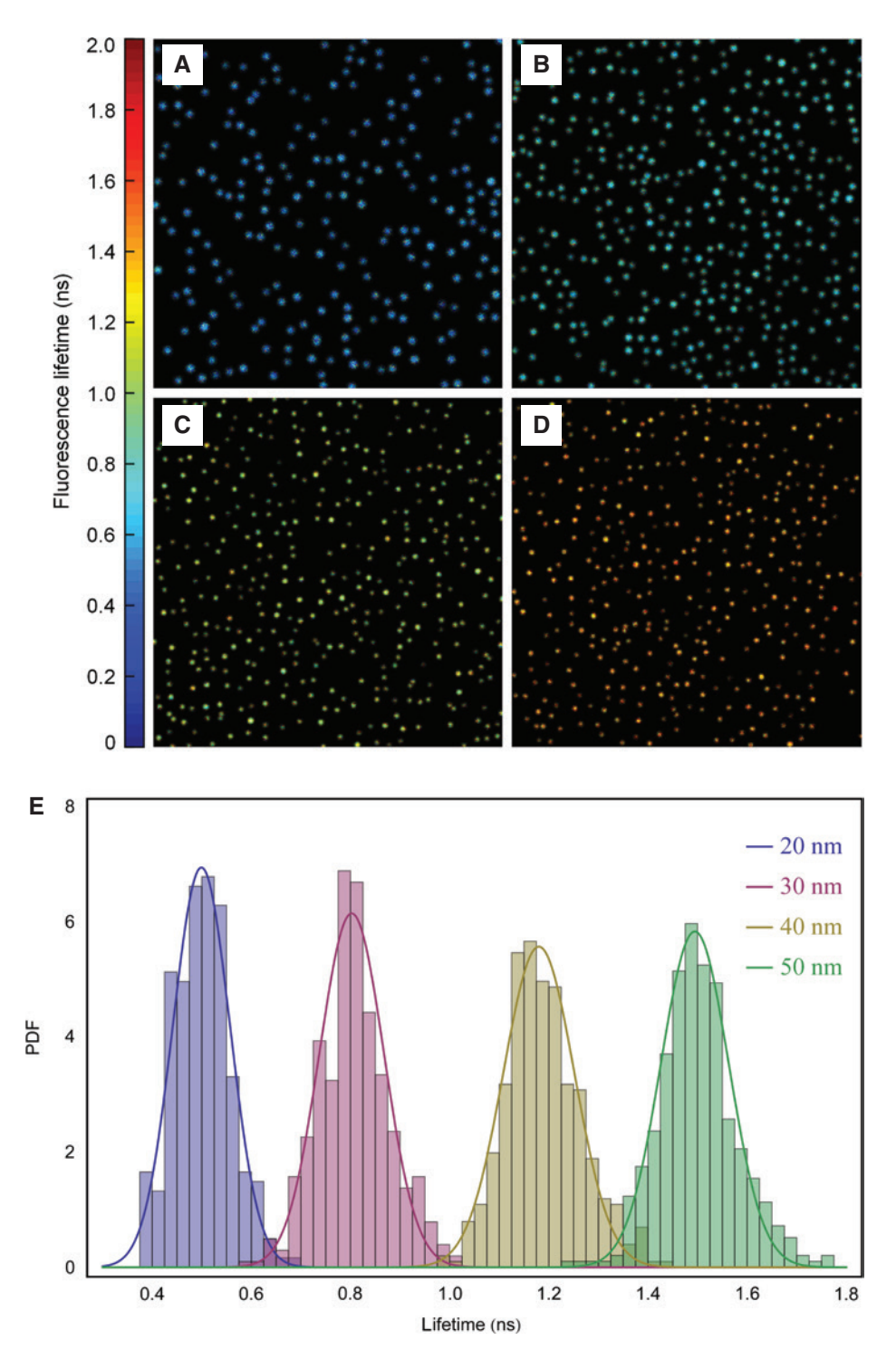


Figure 4: Single-molecule MIET of surface adsorbed fluorescent molecules.

Lifetime images of single Atto 655 molecules (Atto-Tec) spin-coated on MIET substrates with (A) 20 nm, (B) 30 nm, (C) 40 nm, and (D) 50 nm SiO<sub>2</sub> spacer thicknesses. Each image shows a sample area of 30 m × 30 m. The color bar shows the color index for lifetime values in nanoseconds. (E) Lifetime distributions for the four samples. Data taken from [42].

information about the orientation of the emitting molecule. However, the distance range over which smMIET works is much larger than FRET. In the case of smMIET, only the vertical orientation of the emission dipole with respect to the surface is needed, whereas in FRET, three relative orientation angles between donor emission and acceptor absorption dipoles are needed, which are inaccessible by using any independent measurement.

The same group extended the localization of single molecules to all three axes [34]. By splitting the fluorescence between a time-resolved detector and an emCCD camera, it was possible to determine the position and the angular orientation of fixed single molecules with a typical precision of  $\sigma_{xy} \le 4$  nm,  $\sigma_z \le 1$  nm, and  $\sigma_{\phi\theta} \approx 5^{\circ}$ .

In another study the group used MIET to determine three binding positions of a single label on a DNA origami structure [43]. This can be seen as a concept to extend DNA PAINT [44] to the third dimension. With this it is possible to determine label positions with nanometer accuracy in all three dimensions.

The groups of Kaminska and Tinnefeld managed to link well-defined DNA origami structures to a graphene layer [45]. They observed energy transfer of fluorophores attached at distinct positions on the DNA origami to the graphene. The calibration allowed height measurements in the range of 3-60 nm with a precision of about 1 nm.

In a recent publication, Bouchet et al. presented another approach that involves the same principles as MIET [46]. They added a thin ( $d \approx 115$  nm) silver nanowire to the sample. Emitters close to the wire show a reduced fluorescence lifetime. The geometry of the interaction requires more involved modeling to determine the dependence of the lifetime on the distance to the wire.

## 4 Discussion and future perspectives

In the past, MIET has demonstrated its potential to complement super-resolution techniques in fluorescence microscopy. It is fully compatible with classic labeling methods for cells and proteins and does not require any alteration in sample treatment, for example, cell culture or fixation. Therefore, it is easy to implement, versatile, and powerful.

At first sight, the introduction of an absorbing and reflecting gold surface into the microscope seems to be a dreadful idea. It is true that one observes a higher scattering signal from the reflective gold surface. However, since we have a pulsed excitation, the scatter contributes only to the IRF component in the signal and is well discriminated

from the fluorescence due to its temporal signature. The absorption of the gold leads to a decrease in excitation power, which is not critical. However, it does hardly affect the number of detected fluorescence photons. Two reasons explain this effect. At first, the coupling of the electric field to the high refractive index material leads to a drastic change in the distribution of the emission. This way, about 80% of all photons are emitted into the light acceptance cone of the objective. Secondly, the MIET effect enhances the *radiative* rate of the fluorophore. This means that the dve gets brighter and the chance for a transition into the triplet state or for other photo-physical processes is reduced. All this compensates the adverse effects of the gold mirror to a great extent. Moreover, fluorophores that are absorbed on the surface of the substrate are fully quenched by a metal layer. This significantly reduces the background signal.

The next step in the development of MIET is to combine it with wide-field super-resolution methods such as PALM, STORM, and specifically DNA-PAINT. For this, sensitive time-resolved cameras are needed, which are currently in development. Some cameras such as pcoFLIM (PCO AG, Kehlheim, Germany) and LINcam (Photonscore GmbH, Magdeburg, Germany) are already available. In the future, one can expect that single-photon avalanche diode arrays will improve in terms of field of view and homogeneity. These developments will enable 3D super-resolution of fluorophores with an isotropic resolution of 1 nm.

Acknowledgments: The authors thank Sebastian Isbaner, Anna Chizhik, and Daja Ruhlandt for critically reading the manuscript and valuable insights. Funding by the Deutsche Forschungsgemeinschaft (DFG, German Research Foundation) under Germany's Excellence Strategy EXC 2067/1-390729940, and via project A6 of the SFB 860 and projects A5 and A14 of the SFB937 is gratefully acknowledged. Financial support was also provided by the DFG Cluster of Excellence Center for Nanoscale Microscopy and Molecular Physiology of the Brain (CNMPB).

Conflict of Interest: The authors declare no conflict of interest.

#### References

- [1] Purcell EM. Spontaneous transition probabilities in radio-frequency spectroscopy. Phys Rev 1946;69:681.
- [2] Enderlein J. Fluorescence detection of single molecules near a solution/glass interface - an electrodynamic analysis. Chem Phys Lett 1999;308:263-6.

- [3] Enderlein J. Single-molecule fluorescence near a metal layer. Chem Phys 1999;247:1-9.
- [4] Levene MJ, Korlach J, Turner SW, Foguet M, Craighead HG, Webb WW. Zero-mode waveguides for single-molecule analysis at high concentrations. Science 2003;299:682-6.
- [5] Moran-Mirabal JM, Craighead HG. Zero-mode waveguides: subwavelength nanostructures for single molecule studies at high concentrations. Methods 2008;46:11-7.
- [6] Enderlein J. Theoretical study of single molecule fluorescence in a metallic nanocavity. Appl Phys Lett 2002;80:315-7.
- [7] Enderlein J. Spectral properties of a fluorescing molecule within a spherical metallic nanocavity. Phys Chem Chem Phys 2002;4:2780-6.
- [8] Clegg RM. Fluorescence resonance energy transfer. Curr Opin Biotechnol 1995:6:103-10.
- [9] Medintz IL, Hildebrandt N. FRET Förster resonance energy transfer: from theory to applications. Weinheim, Germany, John Wiley & Sons, 2013.
- [10] Drexhage KH, Zwick MM, Kuhn H. Sensibilisierte Fluoreszenz nach strahlungslosem Energieübergang durch dünne Schichten. Ber Bunsenges Phys Chem 1963;67:62-7.
- [11] Bücher H, Drexhage KH, Fleck M, et al. Controlled transfer of excitation energy through thin layers. Mol Cryst 1967;2:199-230.
- [12] Drexhage KH, Fleck M. Wide-angle interference and multipole nature of fluorescence and phosphorescence of organic dyes. Ber Bunsenges Phys Chem 1968;72:330.
- [13] Drexhage KH, Kuhn H, Schäfer FP. Variation of the fluorescence decay time of a molecule in front of a mirror. Ber Bunsenges Phys Chem 1968;72:329.
- [14] Drexhage KH. Influence of a dielectric interface on fluorescence decay time. J Luminescence 1970;2:693-701.
- [15] Drexhage KH. Monomolecular layers and light. Sci Am 1970;222:108-20.
- [16] Drexhage KH. Spontaneous emission rate in the presence of a mirror. In: Mandel L, Wolf E, editors. Coherence and quantum optics. Boston, MA, Springer, 1973:187-90.
- [17] Drexhage KH. Interaction of light with monomolecular dye layers. In: Wolf E, editor. Progress in optics, Vol. 12, Sec. 4. Amsterdam, North-Holland, 1974:163-232.
- [18] Chance RR, Prock A, Silbey RJ. Lifetime of an emitting molecule near a partially reflecting surface. J Chem Phys 1974;60:
- [19] Limozin L, Sengupta K. Quantitative reflection interference contrast microscopy (RICM) in soft matter and cell adhesion. ChemPhysChem 2009;10:2752-68.
- [20] Kukura P, Ewers H, Müller C, Renn A, Helenius A, Sandoghdar V. High-speed nanoscopic tracking of the position and orientation of a single virus. Nat Methods 2009;6:923-7.
- [21] Huang B, Wang W, Bates M, Zhuang X. Three-dimensional super-resolution imaging by stochastic optical reconstruction microscopy. Science 2008;319:810-3.
- [22] Juette MF, Gould TJ, Lessard MD, et al. Three-dimensional sub-100 nm resolution fluorescence microscopy of thick samples. Nat Methods 2008;5:527-9.
- [23] Pavani SRP, Thompson MA, Biteen JS, et al. Three-dimensional, single-molecule fluorescence imaging beyond the diffraction limit by using a double-helix point spread function. Proc Natl Acad Sci USA 2009;106:2995-9.
- [24] Stock K, Sailer R, Strauss WSL, Lyttek M, Steiner R, Schneckenburger H. Variable-angle total internal reflection fluorescence

- microscopy (VA-TIRFM): realization and application of a compact illumination device. J Microsc 2003;211:19-29.
- [25] Cardoso DSM, Déturche R, Vézy C, Jaffiol R. Topography of cells revealed by variable-angle total internal reflection fluorescence microscopy. Biophys J 2016;111:1316-27.
- [26] Ruckstuhl T, Verdes D. Supercritical angle fluorescence (SAF) microscopy. Opt Express 2004;12:4246-54.
- [27] Deschamps J, Mund M, Ries J. 3D superresolution microscopy by supercritical angle detection. Opt Express 2014:22:29081-91.
- [28] Shtengel G, Galbraith JA, Galbraith CG, et al. Interferometric fluorescent super-resolution microscopy resolves 3D cellular ultrastructure. Proc Natl Acad Sci USA 2009;106:3125-30.
- [29] Aquino D, Schönle A, Geisler C, et al. Two-color nanoscopy of three-dimensional volumes by 4pi detection of stochastically switched fluorophores. Nat Methods 2011:8:353-9.
- [30] Szalai AM, Siarry B, Lukin J, et al. Three-dimensional total internal reflection fluorescence nanoscopy with sub-10 nm resolution. bioRxiv 2019; doi: https://doi.org/10.1101/693994.
- [31] Chance RR, Prock A, Silbey RJ. Molecular fluorescence and energy transfer near interfaces. In: Prigogine I, Rice SA, editors. Advance in chemical physics, Vol. 37, Sec. 1. John Wiley & Sons, Inc., 1978:1-65.
- [32] Jackson JD. Classical electrodynamics. New York, NY, USA, John Wiley & Sons, 1999.
- [33] GWDG Project Management Service. Available at: https:// projects.gwdg.de/projects/miet/repository/raw/MIET\_GUI. zip?rev=ZIP.
- [34] Karedla NKVS, Chizhik AM, Stein SC, et al. Three-dimensional single-molecule localization with nanometer accuracy using metal-induced energy transfer (MIET) imaging. J Chem Phys 2018;148:204201.
- [35] Chizhik AI, Gregor I, Ernst B, Enderlein J. Nanocavity-based determination of absolute values of photoluminescence quantum yields. ChemPhysChem 2013;14:505-13.
- [36] Berndt M, Lorenz M, Enderlein J, Diez S. Axial nanometer distances measured by fluorescence lifetime imaging microscopy. Nano Lett 2010;10:1497-500.
- [37] Chizhik AI, Rother J, Gregor I, Janshoff A, Enderlein J. Metalinduced energy transfer for live cell nanoscopy. Nat Photonics 2014;8:124-7.
- [38] Baronsky T, Ruhlandt D, Brückner BR, et al. Cell-substrate dynamics of the epithelial-to-mesenchymal transition. Nano Lett 2017;17:3320-6.
- [39] Chizhik AM, Ruhlandt D, Pfaff J, et al. Three-dimensional reconstruction of nuclear envelope architecture using dualcolor metal-induced energy transfer imaging. ACS Nano 2017;11:11839-46.
- [40] Chizhik AM, Wollnik C, Ruhlandt D, et al. Dual-color metalinduced and Förster resonance energy transfer for cell nanoscopy. Mol Biol Cell 2018;29:846-51.
- [41] Ghosh A, Sharma A, Chizhik AI, et al. Graphene-based metal induced energy transfer for sub-nanometer optical localization. Nat Photonics 2019 (in press).
- [42] Karedla NKVS, Chizhik AI, Gregor I, Chizhik AM, Schulz O, Enderlein J. Single-molecule metal-induced energy transfer (smMIET): resolving nanometer distances at the single-molecule level. ChemPhysChem 2014;15:705-11.
- [43] Isbaner S, Karedla NKVS, Kaminska I, et al. Axial colocalization of single molecules with nanometer accuracy using metalinduced energy transfer. Nano Lett 2018;18:2616-22.

- [44] Jungmann R, Steinhauer C, Scheible M, Kuzyk A, Tinnefeld P, Simmel FC. Single-molecule kinetics and super-resolution microscopy by fluorescence imaging of transient binding on DNA origami. Nano Lett 2010;10:4756-61.
- [45] Kaminska I, Bohlen J, Rocchetti S, Selbach F, Acuna GP, Tinnefeld P. Distance dependence of single-molecule energy transfer
- to graphene measured with DNA origami nano-positioners. Nano Lett 2019;19:4257-62.
- [46] Bouchet D, Scholler J, Blanquer G, De Wilde Y, Izeddin I, Krachmalnicoff V. Probing near-field light-matter interactions with single-molecule lifetime imaging. Optica 2019;6:135-8.